JACS
JOURNAL OF THE AMERICAN CHEMICAL SOCIETY
pubs.acs.org/JACS
Article

Self-passivation of Halide Interstitial Defects by Organic Cations in Hybrid Lead-Halide Perovskites: Ab Initio Quantum Dynamics

Xinbo Ma, Xuesong Tian, Elizabeth Stippell, Oleg V. Prezhdo,* Run Long,* and Wei-Hai Fang

Cite This: J. Am. Chem. Soc. 2024, 146, 29255−29265
Read Online

ABSTRACT: Halide interstitial defects severely hinder the optoelectronic performance of metal halide perovskites, making research on their passivation crucial. We demonstrate, using ab initio nonadiabatic molecular dynamics simulations, that hydrogen vacancies (H_v) at both N and C atoms of the methylammonium (MA) cation in $MAPbI_3$ efficiently passivate iodine interstitials (I_i), providing a self-passivation strategy for dealing with the H_v and I_i defects simultaneously. H_v at the N site ($H_{v\text{-}N}$) introduces a defect state into the valence band, while the state contributed by H_v at the C site ($H_{v\text{-}C}$) evolves from a shallow level at 0 K to a deep midgap state at ambient temperature, exhibiting a high environmental activity. Both $H_{v\text{-}N}$ and $H_{v\text{-}C}$ are strong Lewis bases, capable of capturing and passivating I_i defects. $H_{v\text{-}C}$ is a stronger Lewis base, bonds with I_i better, and exhibits a more pronounced passivation effect. The charge carrier lifetimes in the passivated systems are significantly longer than in those containing either H_v or I_i, and even in pristine $MAPbI_3$. Our demonstration of the H_v and I_i defect self-passivation in $MAPbI_3$ suggests that systematic control of the relative concentrations of H_v and I_i can simultaneously eliminate both types of defects, thereby minimizing charge and energy losses. The demonstrated defect self-passivation strategy provides a promising means for defect control in organic−inorganic halide perovskites and related materials and deepens our atomistic understanding of defect chemistry and charge carrier dynamics in solar energy and optoelectronic materials.

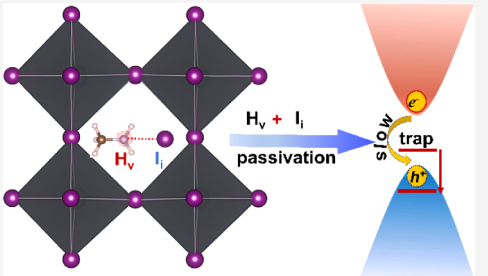

1. INTRODUCTION

Metal halide perovskites have attracted significant attention as a new generation of photovoltaic materials, with their photoelectric conversion efficiency (PCE) rising rapidly over the past decade.[1,2] This high PCE is attributed to their exceptional optoelectronic properties, including tunable band gaps,[3] strong light absorption,[4] long carrier lifetimes, large carrier diffusion lengths,[5] low exciton binding energy,[6,7] and high defect tolerance.[8−10] Cost-effective synthesis methods enhance their appeal further, positioning perovskites as the leading contenders for the next generation of solar materials.[11] Organic−inorganic perovskites have achieved PCE levels of up to 26.2%,[12,13] making them top performers among all perovskite materials.[14−18] However, charge trap states associated with structural defects hinder further advancements in their photoelectric performance.[19−25] Solution processing and rapid crystal growth of perovskite thin films at high temperatures can lead to various types of defects which play crucial roles in charge carrier recombination. In particular, deep-level traps can capture electrons or holes that are unable to escape through thermal activation, leading to nonradiative recombination and significant losses of charge carriers and voltage. Typical deep-level defects in perovskite materials include intrinsic point defects, such as lead interstitial (Pb_i), and antisite defects, e.g., I_{Pb} and Pb_I,[19] three-dimensional defects such as grain boundaries,[26,27] and metal clusters.[28] While shallow-level defects do not trap charges for a long time, they migrate through the device and accumulate at interfaces, initiating interfacial chemical reactions as well as unfavorable band bending and photocurrent hysteresis, which significantly restrict carrier extraction and compromise device stability.[29] Examples of shallow-level defects in organic−inorganic perovskites include intrinsic point defects, such as I, MA, and Pb vacancies, I and MA interstitials, and antisite defects, such as MA_{Pb}.[19] Extensive efforts have been dedicated to mitigating the adverse roles of defects in experiments.[24,30−34]

Chemical passivation is one of the key methods to eliminate defects, stabilize surface and interface structures, and optimize the performance of perovskite solar cells. Passivating molecules can form covalent or ionic bonds with undercoordinated metal cations or halide anions, reducing their chemical activity and ion migration. By eliminating midgap states and facilitating charge separation, passivating species inhibit nonradiative charge recombination. Additives containing Lewis acids and bases can effectively passivate defects in perovskites.[35,36] For instance, under-coordinated iodine atoms can form adducts

Received: September 11, 2024
Revised: October 3, 2024
Accepted: October 4, 2024
Published: October 11, 2024

https://doi.org/10.1021/jacs.4c12634
J. Am. Chem. Soc. 2024, 146, 29255−29265

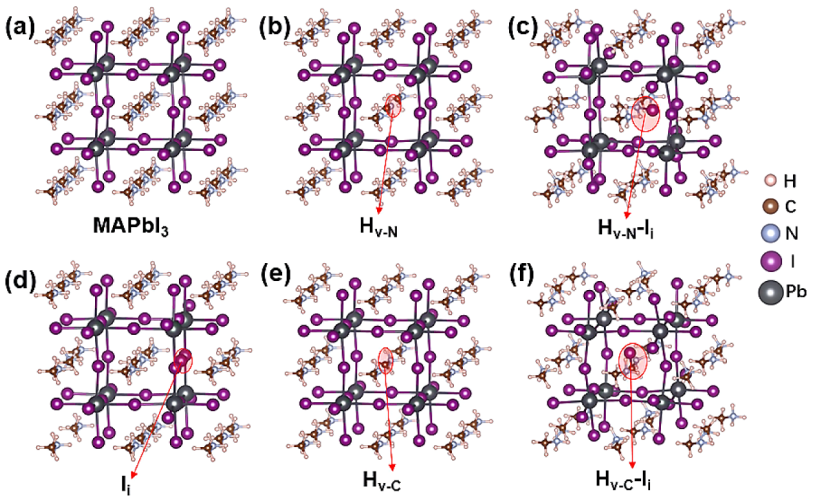

Figure 1. Optimized structures of (a) pristine $MAPbI_3$, (b) $H_{v\text{-}N}$@$MAPbI_3$, (c) $H_{v\text{-}N}I_i$@$MAPbI_3$, (d) I_i@$MAPbI_3$, (e) $H_{v\text{-}C}$@$MAPbI_3$, and (f) $H_{v\text{-}C}I_i$@$MAPbI_3$.

with Lewis base ligands, which create coordinating bonds.[29,36] Yang et al. proposed ligands containing both −NH and −C═O groups could have dual actions. The −NH group would form a hydrogen bond with an iodine atom in a $[PbI_6]^{4-}$ octahedron, simultaneously promoting binding of the −C═O group with the Pb_I antisite defect, to achieve a superior overall passivation effect.[37] Yuan et al. utilized the indigo molecule with both −C═O and −NH groups to achieve efficient chemical passivation of under-coordinated Pb^{2+}/I_i and Pb_I antisite defects and improved device stability under heat and moisture stresses.[38] Gao's group demonstrated that Lewis bases with protonated functional groups possess stronger chemical passivation capabilities compared to those with only Lewis base groups.[39] Our previous studies, employing ab initio quantum dynamics simulations of excited state processes, have elucidated the mechanisms of passivation of point defects, including iodine vacancies (I_v), I_i, and lead interstitials (Pb_i), by Lewis acids, bases, alkali metals, oxygen, water and strain.[40−49] We have demonstrated the positive influence of halogen atoms and alkali metals in the passivation of extended defects, such as perovskite grain boundaries.[50,51] Recent theoretical studies have expanded the scope to include deep-level defects originating from hydrogen vacancies (H_v) and hydrogen interstitials (H_i) in organic−inorganic perovskites.[33,52] Zhang et al. illustrated that H_v defects can exist in the prototypical hybrid perovskite $MAPbI_3$ and function as highly efficient nonradiative recombination centers, exhibiting an exceptionally high carrier capture coefficient.[33] Liang et al. established that H_i defects, which are prevalent under both iodine-rich and iodine-poor conditions in $FAPbI_3$, serve as potent nonradiative recombination centers.[52] It is known that when MA loses a hydrogen, the unpaired electron on N or C exhibits a certain Lewis basicity. Meanwhile, the nonbonding I_i defect is capable of accepting electrons. Consequently, H_v can potentially capture I_i defects and eliminate the trap states in $MAPbI_3$. Important for practical applications of perovskites, this hypothesis requires a theoretical confirmation.

In this study, we systematically investigate the self-passivation strategy by which the H_v and I_i defects in $MAPbI_3$ can eliminate or passivate each other. Using ab initio nonadiabatic molecular dynamics, we demonstrate that $H_{v\text{-}N}$ introduces a shallow defect level into the valence band, whereas the defect state formed by $H_{v\text{-}C}$ evolves from shallow at low temperatures to deep at ambient temperatures, displaying high environmental activity. Both $H_{v\text{-}N}$ and $H_{v\text{-}C}$ defects demonstrate significant Lewis basicity and effectively capture I_i through bonding interactions, thereby passivating the H_v and I_i defects simultaneously. $H_{v\text{-}C}$ exhibits a higher environmental activity and Lewis basicity than $H_{v\text{-}N}$, resulting in stronger bonding with I_i and creating a more pronounced passivation effect. The carrier lifetimes of the H_v-passivated systems are notably longer than those of the unpassivated systems and even pristine $MAPbI_3$. Our results demonstrate that H_v defects in $MAPbI_3$ effectively passivate I_i defects, suggesting that systematic control of the relative concentrations of H_v and I_i can simultaneously eliminate both types of defects, and decrease charge and energy losses. The self-passivation strategy provides a promising avenue of research into control of defects in organic−inorganic halide perovskites and related materials and further advances our understanding of defect chemistry in optoelectronic and solar energy devices.

2. SIMULATION DETAILS

The nonadiabatic (NA) molecular dynamics (MD)[53−57] simulations are performed with the decoherence induced surface hopping (DISH) method,[58,59] which is implemented within the time-dependent Kohn−Sham density functional theory.[60,61] The lighter and faster electrons are described quantum mechanically, while the heavier and slower nuclei are treated semiclassically. DISH takes into consideration quantum decoherence of the electronic subsystem.[58,59,62−64] The decoherence time is estimated as the pure-dephasing time derived from the optical response theory.[65] Quantum transitions take place in the DISH algorithm as a result of the decoherence process and take place at decoherence effects, establishing the physical foundation for the hops.[58,59,62−64] The classical path approximation is employed, rationalized by the observation that thermal fluctuations in atomic coordinates are more pronounced compared to geometry differences between ground and excited states.[62,66] The NA-MD methodology has been successfully applied to investigate photoexcitation dynamics in various systems.[67−76]

All electronic structure calculations are conducted utilizing density functional theory (DFT) implemented within the

https://doi.org/10.1021/jacs.4c12634
J. Am. Chem. Soc. 2024, 146, 29255−29265

Vienna ab initio simulation package (VASP).[77] The core electrons are described with the projector-augmented wave (PAW) method.[78] The generalized gradient approximation (GGA) for the exchange-correlation functional developed by Perdew, Burke, and Ernzerhof (PBE) is utilized.[79] A plane wave energy cutoff of 500 eV and Γ-centered 3 × 3 × 1 Monkhorst−Pack k-point mesh[80] are used. van der Waals interactions are described using the Grimme DFT-D3 method.[81] After an initial geometry optimization at 0 K, the systems are heated to 300 K through repeated velocity rescaling. Subsequently, 6 ps of adiabatic MD trajectories are generated with a time step of 1 fs and are used for calculating the NA couplings.[82,83] The NA Hamiltonian derived from the 6 ps trajectory is iterated multiple times to provide input for the DISH algorithm. Only the Γ-point is used for NA-MD calculations, since $MAPbI_3$ has a direct band gap at the Γ-point and the defects create localized states with flat k-point dependence. All 6,000 geometries from the trajectory are used as the initial conditions for the DISH algorithm, and 100 random number sequences are sampled for each initial condition. The NA-MD calculations are performed using the PYXAID software package.[62,66]

3. RESULTS AND DISCUSSION

3.1. Geometric Structure. The cubic phase of α-$MAPbI_3$ was used to create (2 × 2 × 2) supercells. We consider six systems: pristine $MAPbI_3$, $MAPbI_3$ with the I_i defect (I_i@$MAPbI_3$), $MAPbI_3$ with the H_v defects at the N site ($H_{v\text{-}N}$@$MAPbI_3$) and the C site ($H_{v\text{-}C}$@$MAPbI_3$), and $MAPbI_3$ with the I_i defect passivated by H_{v-N} and $H_{v\text{-}C}$ ($H_{v\text{-}N}I_i$@$MAPbI_3$ and $H_{v\text{-}C}I_i$@$MAPbI_3$, respectively). The optimized structures of these systems are shown in Figure 1. The presence of H_v shortens the C−N bond of the MA molecule. The C−N(H_v) and C(H_v)−N distances are 1.435 and 1.439 Å in $H_{v\text{-}N}$@$MAPbI_3$, and $H_{v\text{-}C}$@$MAPbI_3$, respectively, smaller than that in pristine $MAPbI_3$ (1.492 Å). The shortening of the C−N bond can be explained by the fact that when the MA molecule loses an H atom, the interaction between the C and N atoms is enhanced, leading to the bond contraction. In $H_{v\text{-}N}I_i$@$MAPbI_3$ and $H_{v\text{-}C}I_i$@$MAPbI_3$, the N and C atoms at the H_v sites both undergo strong bonding interactions with I_i. This bonding interaction between H_v and I_i significantly elongates the C−N bond. The C−N(H_v) and C(H_v)−N distances increase by nearly half an angstrom, to 1.473 and 1.484 Å in $H_{v\text{-}N}I_i$@$MAPbI_3$ and $H_{v\text{-}C}I_i$@$MAPbI_3$, compared to $H_{v\text{-}N}$@$MAPbI_3$ and $H_{v\text{-}C}$@$MAPbI_3$, respectively. The C(H_v)−I_i distance in $H_{v\text{-}C}I_i$@$MAPbI_3$ (2.147 Å) is smaller than N(H_v)−I_i (2.268 Å) in $H_{v\text{-}N}I_i$@$MAPbI_3$, pointing to a stronger interaction between C(H_v) and I_i. This indicates that the Lewis basicity of $H_{v\text{-}C}$ is stronger than that of $H_{v\text{-}N}$.

Thermal motions of H_v within the MA molecule induce substantial fluctuations in the C−N, N(H_v)−I_i and C(H_v)−I_i distances. At 300 K, the canonically averaged C−N distance in pristine $MAPbI_3$ is 1.497 Å, larger than at 0 K (1.492 Å). In $H_{v\text{-}N}$@$MAPbI_3$ and $H_{v\text{-}C}$@$MAPbI_3$, the canonically averaged C−N(H_v) and C(H_v)−N distances increase to 1.446 and 1.481 Å, respectively, relative to 1.435 and 1.439 Å at 0 K. The interactions of $H_{v\text{-}N}$ and $H_{v\text{-}C}$ with the surrounding Pb−I framework are enhanced, and the fluctuations of the length of the C−N bond in the MA molecules are also enhanced, compared to pristine $MAPbI_3$ (Figure S1). The statistical distributions of the ∠Pb−I−Pb bond angles near H_v are shown in Figure S2. The distribution in $H_{v\text{-}N}$@$MAPbI_3$ is much narrower than in $H_{v\text{-}C}$@$MAPbI_3$, indicating larger distortions and fluctuations of the $[PbI_6]^{4-}$ octahedra in $H_{v\text{-}C}$@$MAPbI_3$. This can be attributed to hydrogen bonding interactions between N(H_v) and the surrounding I atoms in $H_{v\text{-}N}$@$MAPbI_3$, which make the Pb−I framework relatively more stable compared to $H_{v\text{-}C}$@$MAPbI_3$.

The defect formation energy of $H_{v\text{-}C}$@$MAPbI_3$ (2.305 eV) is significantly higher than that of $H_{v\text{-}N}$@$MAPbI_3$ (1.520 eV), indicating that it is more difficult for the $-CH_3$ group of the MA molecule to lose a hydrogen atom compared to the $-NH_3$ group. Therefore, once the $-CH_3$ group loses a hydrogen atom, it becomes more active to the environment. This corresponds to the stronger Lewis basicity in the $H_{v\text{-}C}$ system. The evolutions of the N(H_v)−I_i and C(H_v)−I_i bond lengths are shown in Figure 2a. The corresponding canonically

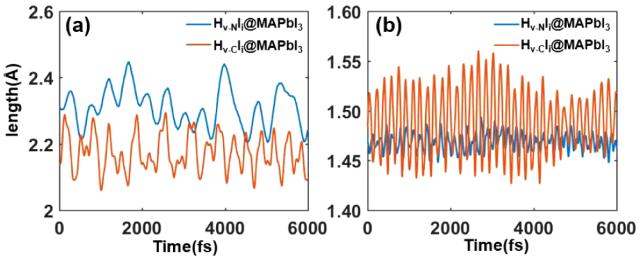

Figure 2. Evolutions of (a) N(H_v)−I_i and C(H_v)−I_i distances in $H_{v\text{-}N}I_i$@$MAPbI_3$ and $H_{v\text{-}C}I_i$@$MAPbI_3$. (b) Evolutions of C−N(H_v) and C(H_v)−N distances in $H_{v\text{-}N}I_i$@$MAPbI_3$ and $H_{v\text{-}C}I_i$@$MAPbI_3$.

averaged N(H_v)−I_i and C(H_v)−I_i distances are 2.310 and 2.173 Å, indicating bonding interactions between either N or C and I_i in these systems. The distance between C(H_v) and I_i is significantly smaller than between N(H_v) and I_i, indicating that the bonding interaction between C(H_v) and I_i is stronger. Due to the strong interaction between H_v and I_i, the defect formation energies of both $H_{v\text{-}N}I_i$@$MAPbI_3$ and $H_{v\text{-}C}I_i$@$MAPbI_3$ are significantly reduced to 0.345 and 0.090 eV, respectively, indicating that H_v defects can easily capture I_i. The lower defect formation energy of $H_{v\text{-}C}I_i$@$MAPbI_3$ compared to $H_{v\text{-}N}I_i$@$MAPbI_3$ suggests that $H_{v\text{-}C}$ exhibits a stronger Lewis basicity and has a greater passivation effect compared to $H_{v\text{-}N}$. The stronger interaction between C(H_v) and I_i in $H_{v\text{-}C}I_i$@$MAPbI_3$ than $H_{v\text{-}N}I_i$@$MAPbI_3$ disturbs the C−N bond more, causing a greater fluctuation and a larger average value of the C−N bond length (Figure 2b). This results in a greater distortion of the Pb−I framework in $H_{v\text{-}C}I_i$@$MAPbI_3$ compared to $H_{v\text{-}N}I_i$@$MAPbI_3$ during the dynamics evolution. Seen from Figure S3, the ∠Pb−I−Pb bond angle in $H_{v\text{-}C}I_i$@$MAPbI_3$ is significantly smaller than in $H_{v\text{-}N}I_i$@$MAPbI_3$, indicating a greater distortion of the $[PbI_6]^{4-}$ octahedra in $H_{v\text{-}C}I_i$@$MAPbI_3$. The distortion of the $[PbI_6]^{4-}$ octahedra can be expected to correlate with an enhanced charge localization, decreasing electron−hole interactions and leading to a slower carrier recombination.

The standard deviations in atomic positions, presented in Table 1, offer a quantitative measure of lattice stability and the extent of thermal vibrations within each system. These values are computed using the formula $\sigma_i = \sqrt{\langle (r_i - r_i)^2 \rangle}$, where r_i denotes the position of atom i, and the angular brackets signify averaging over the 6 ps adiabatic MD trajectories and a specific group of atoms. Larger standard deviations indicate increased atomic motions. After an MA molecule loses a hydrogen atom,

https://doi.org/10.1021/jacs.4c12634
J. Am. Chem. Soc. 2024, 146, 29255−29265

Table 1. Standard Deviations (Å) of the Positions of MA, Pb−I Atoms in Pristine $MAPbI_3$, I_i@$MAPbI_3$, $H_{v\text{-}N}$@$MAPbI_3$, $H_{v\text{-}C}$@$MAPbI_3$, $H_{v\text{-}N}I_i$@$MAPbI_3$, and $H_{v\text{-}C}I_i$@$MAPbI_3$

	$MAPbI_3$	I_i@$MAPbI_3$	$H_{v\text{-}N}$@$MAPbI_3$	$H_{v\text{-}C}$@$MAPbI_3$	$H_{v\text{-}N}I_i$@$MAPbI_3$	$H_{v\text{-}C}I_i$@$MAPbI_3$
MA	0.876	0.845	0.892	0.920	0.852	0.780
Pb−I	0.352	0.419	0.422	0.408	0.430	0.426

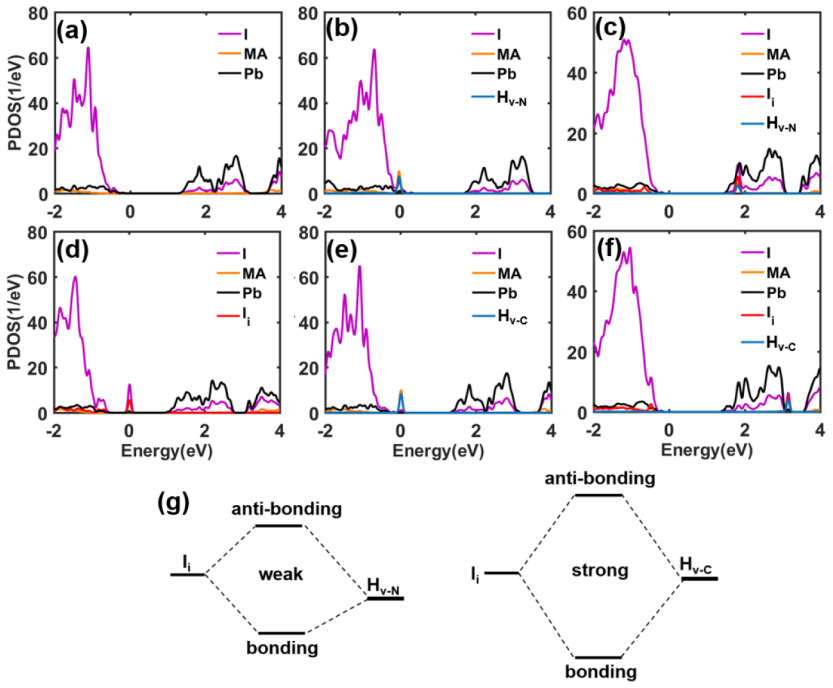

Figure 3. Projected densities of states (PDOS) of (a) pristine $MAPbI_3$, (b) $H_{v\text{-}N}$@$MAPbI_3$, (c) $H_{v\text{-}N}I_i$@$MAPbI_3$, (d) I_i@$MAPbI_3$, (e) $H_{v\text{-}C}$@$MAPbI_3$, and (f) $H_{v\text{-}C}I_i$@$MAPbI_3$. (g) Schematics of orbital hybridization in $H_{v\text{-}N}I_i$@$MAPbI_3$ and $H_{v\text{-}C}I_i$@$MAPbI_3$.

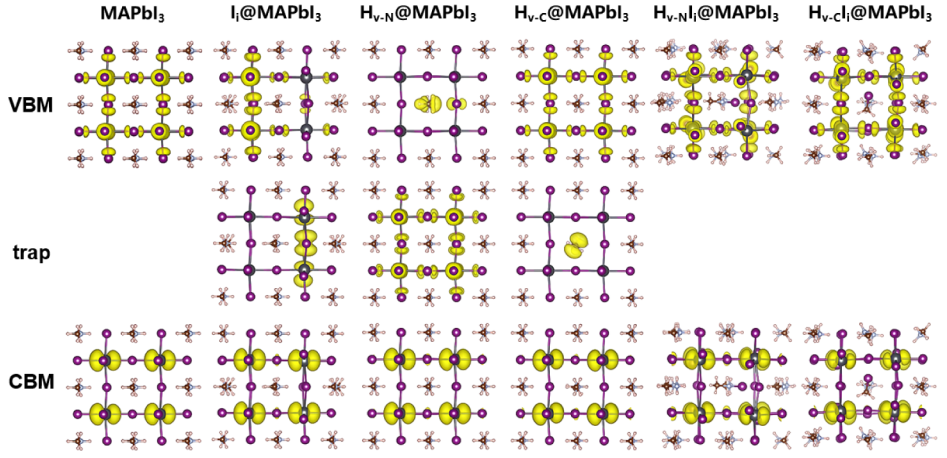

Figure 4. Charge densities of the VBM, trap and CBM states in pristine $MAPbI_3$, I_i@$MAPbI_3$, $H_{v\text{-}N}$@$MAPbI_3$, $H_{v\text{-}C}$@$MAPbI_3$, $H_{v\text{-}N}I_i$@$MAPbI_3$, and $H_{v\text{-}C}I_i$@$MAPbI_3$.

the reduced steric hindrance results in an increased atomic movement of the MA molecule in both $H_{v\text{-}N}$@$MAPbI_3$ and $H_{v\text{-}C}$@$MAPbI_3$. This enhanced movement impacts the Pb−I framework, causing its atomic fluctuations to increase as well. However, when the MA molecule interacts with I_i, the steric hindrance significantly increases, leading to a decrease in the atomic movement of the MA molecule in both $H_{v\text{-}N}I_i$@$MAPbI_3$ and $H_{v\text{-}C}I_i$@$MAPbI_3$. At the same time, the C(H_v)−N bond in $H_{v\text{-}C}I_i$@$MAPbI_3$ fluctuates more than the C−N(H_v) bond in $H_{v\text{-}N}I_i$@$MAPbI_3$, Figure 2b. The atomic movements of the Pb−I framework in the passivated systems ($H_{v\text{-}N}I_i$@$MAPbI_3$ and $H_{v\text{-}C}I_i$@$MAPbI_3$) are greater than in pristine $MAPbI_3$ due to the larger distortion of the Pb−I framework. A greater atomic movement is correlated with a faster decoherence process, generally leading to a longer carrier lifetime.

3.2. Electronic Structure. Figure 3 presents the projected density of states (PDOS) for the six systems under consideration. In pristine $MAPbI_3$, the valence band maximum (VBM) is contributed by atomic orbitals of Pb and I atoms,

https://doi.org/10.1021/jacs.4c12634
J. Am. Chem. Soc. 2024, 146, 29255−29265

while the conduction band minimum (CBM) is predominantly composed of Pb atomic orbitals. The defect state in $H_{v\text{-}N}$@$MAPbI_3$ resides within the valence band (VB), whereas the defect state in $H_{v\text{-}C}$@$MAPbI_3$ is within the band gap and relatively close to the VB. Similarly, in I_i@$MAPbI_3$, the defect state contributed by I_i is also within the band gap and close to the VB, resembling the behavior observed in $H_{v\text{-}C}$@$MAPbI_3$. The charge densities of the key states in these systems are shown in Figure 4. The charge density of the VBM concentrates on I and Pb atoms, whereas the charge density of the CBM primarily localizes on the Pb atoms in pristine $MAPbI_3$. In $H_{v\text{-}N}$@$MAPbI_3$, the VBM charge density is localized around $H_{v\text{-}N}$, while in $H_{v\text{-}C}$@$MAPbI_3$ the trap state is localized around $H_{v\text{-}C}$ and the VBM charge density is comparable to the pristine structure. It can be observed from the PDOS that the states localized around $H_{v\text{-}N}$ and $H_{v\text{-}C}$ mainly originate from N-p and C-p orbitals, with only a small portion contributed by Pb-p. Therefore, the Pb-p component is not visible in the charge density of these states. In I_i@$MAPbI_3$, the trap state is localized around I_i, decreasing the charge density around the defect at the VBM. However, when the H_v vacancy captures I_i in $H_{v\text{-}N}I_i$@$MAPbI_3$ and $H_{v\text{-}C}I_i$@$MAPbI_3$, the charge densities of the VBM and CBM align with those of pristine $MAPbI_3$. Figure 5a,c shows the projected band structures (PBAND) for $H_{v\text{-}N}$@$MAPbI_3$ and $H_{v\text{-}C}$@$MAPbI_3$. The states contributed by $H_{v\text{-}N}$ and $H_{v\text{-}C}$ both exhibit flat bands characteristic of localized states. The flat band contributed by $H_{v\text{-}N}$ is within the valence band in $H_{v\text{-}N}$@$MAPbI_3$, while the flat band contributed by $H_{v\text{-}C}$ is within the band gap in $H_{v\text{-}C}$@$MAPbI_3$ like in the PDOS. The orbital hybridization diagrams (Figure 5b,d) reveal that both flat bands are mainly contributed by the 2p orbitals of N(C) hybridized with the 6p orbitals of Pb. Since the energy level of the 2p orbital of C is higher than that of the 2p orbital of N, the flat band contributed by $N(H_v)$ is located within the VB, whereas the flat band contributed by $H_{v\text{-}C}$ is situated within the band gap. Furthermore, as the band contributed by $H_{v\text{-}N}$ sinks into the VB, a dispersive band emerges above it. Since the band is derived from Pb and I and exhibits high dispersion, it is delocalized, as evidenced by the charge density, Figure 4.

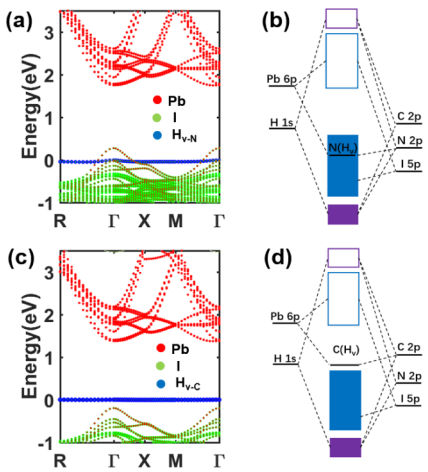

Figure 5. (a) Projected band structure and (b) schematic of atomic orbital hybridization in $H_{v\text{-}N}$@$MAPbI_3$. (c) Projected band structure and (d) schematic of atomic orbital hybridization in $H_{v\text{-}C}$@$MAPbI_3$.

The evolutions of the VBM, CBM, and trap state energies for $H_{v\text{-}N}$@$MAPbI_3$ and $H_{v\text{-}C}$@$MAPbI_3$ are shown in Figure S4. The energy level contributed by $H_{v\text{-}N}$ evolves within the VB, close to the VBM. The energy level contributed by $H_{v\text{-}C}$ undergoes significant fluctuation during its evolution, with a substantial portion evolving deep into the band gap. Deep-level defect states facilitate nonradiative recombination, leading to severe energy and charge losses. In $H_{v\text{-}N}I_i$@$MAPbI_3$ and $H_{v\text{-}C}I_i$@$MAPbI_3$, both $N(H_v)$ and $C(H_v)$ undergo bonding interactions with I_i. This results in the trap defect states sinking into the valence and conduction bands (Figure 3c,f). It can be observed that the energy levels of the states contributed by $H_{v\text{-}C}$ are closer to I_i than those of $H_{v\text{-}N}$ (Figure 3b,d,e). This favors a stronger bonding interaction between $C(H_v)$ and I_i (Figure 3g), leading to the shorter length of the $C(H_v)$–I_i bond in $H_{v\text{-}C}I_i$@$MAPbI_3$.

3.3. Electron–Vibrational Interactions. Vibrational motions play an essential role during the charge trapping and recombination processes. They provide the NA coupling that initiates these processes, and accommodate the excess electronic energy released during the nonradiative relaxation. The NA coupling values are summarized in Table 2. To identify the key vibrational modes, we calculate the electron-vibrational spectral densities by performing Fourier transforms of the autocorrelation function of fluctuations of the energy gaps between each pair of the key states (Figure 6). The spectral densities in all six systems exhibit signals in the low-frequency region below 400 cm^{-1}. The peak at 100 cm^{-1} can be attributed to the stretching mode of the inorganic Pb–I

Table 2. Canonically Averaged Energy Gaps, Absolute NA Couplings, Pure-Dephasing Times, and Transition Rate Constants in Pristine $MAPbI_3$, I_i@$MAPbI_3$, $H_{v\text{-}N}$@$MAPbI_3$, $H_{v\text{-}C}$@$MAPbI_3$, $H_{v\text{-}N}I_i$@$MAPbI_3$, and $H_{v\text{-}C}I_i$@$MAPbI_3$

		Gap (eV)	NA coupling (meV)	Dephasing (fs)	Rate (ns^{-1})
$MAPbI_3$	CBM → VBM	1.60	0.94	7.34	0.44
I_i@$MAPbI_3$	CBM → VBM	1.76	0.89	6.19	0.29
	trap → VBM	0.34	4.59	7.00	52.14
	CBM → trap	1.42	0.61	5.05	0.72
$H_{v\text{-}N}$@$MAPbI_3$	CBM → VBM	1.81	0.84	6.13	0.28
	trap → VBM	0.19	6.33	10.45	170.79
	CBM → Trap	1.62	0.95	6.83	0.61
$H_{v\text{-}C}$@$MAPbI_3$	CBM → VBM	1.84	0.57	7.12	0.25
	trap → VBM	0.74	1.93	2.89	11.78
	CBM → Trap	1.10	2.07	2.66	8.80
$H_{v\text{-}N}I_i$@$MAPbI_3$	CBM → VBM	1.73	0.71	3.03	0.37
$H_{v\text{-}C}I_i$@$MAPbI_3$	CBM → VBM	1.78	0.60	5.15	0.30

https://doi.org/10.1021/jacs.4c12634
J. Am. Chem. Soc. 2024, 146, 29255–29265

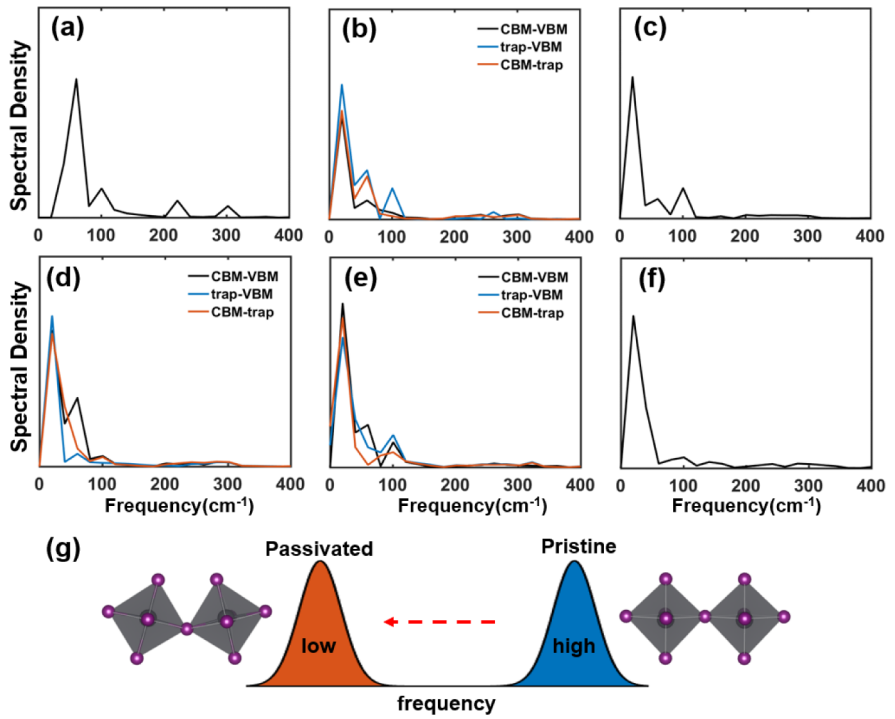

Figure 6. Fourier transforms of autocorrelation functions of phonon-induced fluctuations of energy gaps in (a) pristine $MAPbI_3$, (b) $H_{v\text{-}N}$@$MAPbI_3$, (c) $H_{v\text{-}N}I_i$@$MAPbI_3$, (d) I_i@$MAPbI_3$, (e) $H_{v\text{-}C}$@$MAPbI_3$, and (f) $H_{v\text{-}C}I_i$@$MAPbI_3$. (g) Diagram of frequency difference in the pristine and passivated systems. The larger distortion of $[PbI_6]^{4-}$ in the passivated systems leads to a red-shift in frequency.

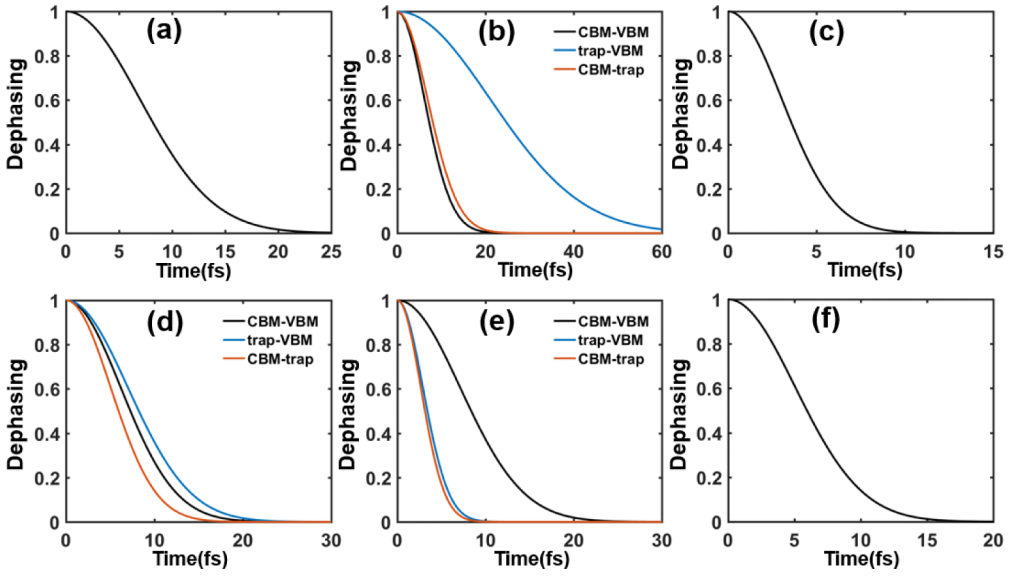

Figure 7. Pure-dephasing functions for the key pairs of states in (a) pristine $MAPbI_3$, (b) $H_{v\text{-}N}$@$MAPbI_3$, (c) $H_{v\text{-}N}I_i$@$MAPbI_3$, (d) I_i@$MAPbI_3$, (e) $H_{v\text{-}C}$@$MAPbI_3$, and (f) $H_{v\text{-}C}I_i$@$MAPbI_3$.

lattice.[84] The dominant peak below 60 cm^{-1} is ascribed to Pb−I−Pb bending.[85] In the presence of H_v, the Pb−I−Pb distortion around H_v increases, enhancing the contribution of vibrations in the low-frequency region below 100 cm^{-1}. In $H_{v\text{-}N}I_i$@$MAPbI_3$ and $H_{v\text{-}C}I_i$@$MAPbI_3$, the formation of the large MA-I group due to the bonding of N(H_v) and C(H_v) with I_i causes further distortion of the surrounding $[PbI_6]^{4-}$ octahedra, also resulting in enhanced vibrations in the low-frequency region below 100 cm^{-1}. Additionally, the low-frequency vibrations of the passivated systems are red-shifted overall (Figure 6g). Since the NA coupling is proportional to atomic velocity and the velocity decreases with decreasing vibrational frequency, the red-shift rationalizes the weakening of the NA coupling in $H_{v\text{-}N}I_i$@$MAPbI_3$ and $H_{v\text{-}C}I_i$@$MAPbI_3$ compared to pristine $MAPbI_3$. The greater distortion of Pb−I−Pb in $H_{v\text{-}C}I_i$@$MAPbI_3$ compared to $H_{v\text{-}N}I_i$@$MAPbI_3$ results in a stronger peak intensity around 30 cm^{-1} in $H_{v\text{-}C}I_i$@$MAPbI_3$ and increased charge localization, thereby reducing the NA coupling. The higher frequency modes in the range of 150−200 cm^{-1} are linked to the vibrations of MA molecules.[84] The peaks at 300 and 400 cm^{-1} correspond to MA torsional modes.[84] The introduction of H_v and I_i leads to a significant

https://doi.org/10.1021/jacs.4c12634
J. Am. Chem. Soc. 2024, 146, 29255−29265

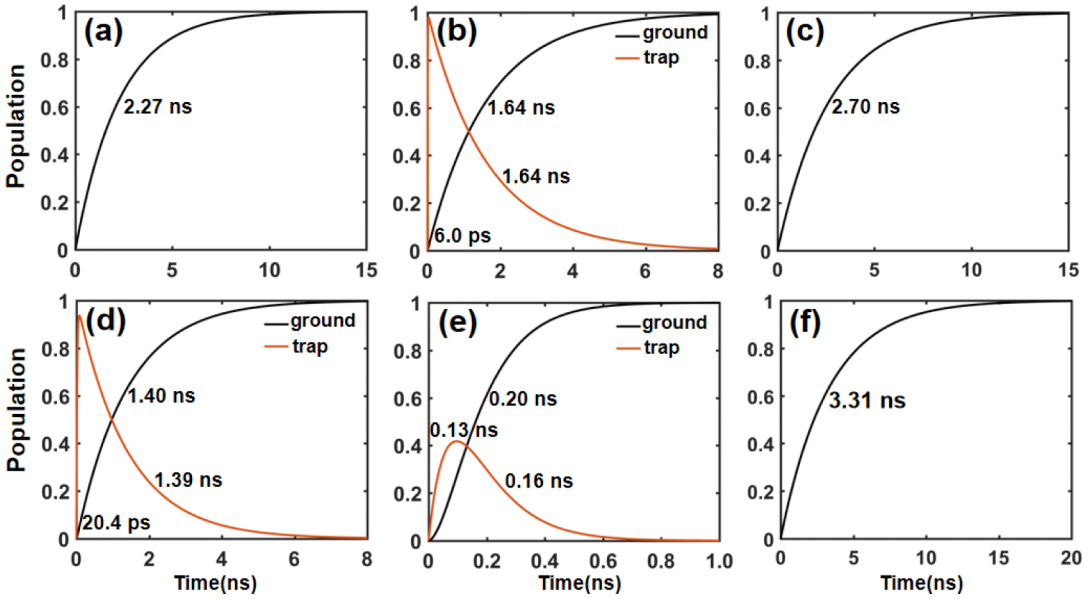

Figure 8. Evolution of populations of the key states in (a) pristine $MAPbI_3$, (b) $H_{v\text{-}N}$@$MAPbI_3$, (c) $H_{v\text{-}N}I_i$@$MAPbI_3$, (d) I_i@$MAPbI_3$, (e) $H_{v\text{-}C}$@$MAPbI_3$, and (f) $H_{v\text{-}C}I_i$@$MAPbI_3$.

increase in the distortion of the Pb−I framework. This reduces the relative motion of MA with respect to the Pb−I framework (Table 1), resulting in a notable reduction of the signals in the high-frequency region in the defect and passivated systems.

The NA electron-vibrational coupling is responsible for inelastic scattering events leading to an electron-vibrational energy exchange. Elastic scattering causes loss of coherence within the electronic subsystem and is known as the pure-dephasing process. The pure-dephasing functions calculated using the second-order cumulant expansion based on the optical response theory are presented in Figure 7. The pure-dephasing times are obtained by fitting the curves to a Gaussian function, $e^{-0.5(t/\tau)^2}$. A quantum mechanical wave packet representing the entire electron-vibrational system splits into uncorrelated branches, and the electronic subsystem loses coherence due to coupling to vibrations. This resulting decoherence can be understood as an environment-induced collapse of superposed quantum electronic states. For a quantum transition between two states to occur, their wave functions must form a coherent superposition. If coherence between the state is lost rapidly, it can significantly hinder or even completely prevent the quantum transition.[58] In all cases, coherence loss occurs on a 10 fs time scale, much faster than the charge trapping and recombination processes. The pure-dephasing time for the CBM-VBM transition is 7.34 fs in pristine $MAPbI_3$. The enhanced randomness and disorder due to the introduction of defects accelerates coherence loss further. As a result, the pure-dephasing times for the CBM-VBM transitions are even shorter in $H_{v\text{-}N}$@$MAPbI_3$, $H_{v\text{-}C}$@$MAPbI_3$ and I_i@$MAPbI_3$ (Table 2). In $H_{v\text{-}N}I_i$@$MAPbI_3$ and $H_{v\text{-}C}I_i$@$MAPbI_3$, $N(H_v)$ or $C(H_v)$ undergo bonding interactions with I_i, resulting in the formation of large MA-I moieties that have a strong influence on the motions of the Pb−I lattice, further accelerating decoherence. The pure-dephasing times for the CBM-VBM transition decrease to 3.03 and 5.15 fs in $H_{v\text{-}N}I_i$@$MAPbI_3$ and $H_{v\text{-}C}I_i$@$MAPbI_3$, respectively. Typically, faster decoherence leads to slower carrier recombination.[63]

3.4. Nonradiative Electron−Hole Recombination. The nonradiative charge recombination occurs on nanosecond time scales, exceeding capabilities of ab initio NA-MD. Machine learning tools can be employed to extend NA-MD simulation time and size.[86,87] In the present work, we use 6 ps NA-MD trajectories to obtain rates of transitions between the key states and use the rates in the corresponding kinetic equations (eqs S1−S3). The solutions to the kinetic equations can be represented through analytic expressions (eqs S4−S6) for the state populations. The results of the state-to-state NA-MD simulations are shown in Figure S6, and the rates are obtained by exponential fits to the data.

The energy levels of the trap states in the I_i@$MAPbI_3$ and $H_{v\text{-}N}$@$MAPbI_3$ systems are relatively shallow and are located near the VBM. They act as hole traps, with hole trapping taking 20.4 and 6.0 ps in I_i@$MAPbI_3$ and $H_{v\text{-}N}$@$MAPbI_3$, respectively (Figure 8b,d). The trapped hole recombines with an electron in the CBM on a nanosecond time scale. The trap states within the band gap accelerate the electron−hole recombination time to 1.40 and 1.64 ns in I_i@$MAPbI_3$ and $H_{v\text{-}N}$@$MAPbI_3$, respectively, compared to pristine $MAPbI_3$ (2.27 ns). Because the trap level in $H_{v\text{-}C}$@$MAPbI_3$ evolves deep into the band gap, the charge trapping and subsequent recombination processes occur on comparable time scales, 0.13 and 0.16 ns, respectively (Figure 8e). The rate-limiting step of carrier recombination via trap states is the slower recombination across a large gap between the trap state and the "opposite" band edge. Therefore, deep-level traps accelerate carrier recombination significantly compared to shallow-level defects (Figure S7), since the gaps to the trap level from both the VBM and the CBM are significantly smaller than the VBM−CBM band gap. This increase in trap level energy in deep-level traps decreases the charge transfer rate for the rate-limiting step. Consequently, the presence of the deep-level defect makes the nonradiative recombination an order of magnitude faster (0.20 ns) in $H_{v\text{-}C}$@$MAPbI_3$ than the other systems. The charge recombination is the slowest in the self-passivated $H_{v\text{-}N}I_i$@$MAPbI_3$ and $H_{v\text{-}C}I_i$@$MAPbI_3$ systems with time scales of 2.70 and 3.31 ns, respectively (Figure 8c,f). The

https://doi.org/10.1021/jacs.4c12634
J. Am. Chem. Soc. 2024, 146, 29255−29265

passivation of I_i by H_v eliminates the nonradiative recombination centers, while, at the same time, enhances localization of the band-edge states due to the larger distortion of the Pb−I framework, leading to a reduction in the NA coupling and shortening of the coherence time, thereby making the charge carrier lifetimes longer. The NA-MD simulations reveal that $H_{v\text{-}C}$ gives a more effective passivation of I_i than $H_{v\text{-}N}$ due to the stronger Lewis basicity of $H_{v\text{-}C}$ compared to $H_{v\text{-}N}$ in $MAPbI_3$. Both I_i and $H_{v\text{-}C}$ introduce deep defect levels, and their pairing results in simultaneous passivation of both defects.

4. CONCLUSION

To recapitulate, we have investigated systematically self-passivation of hydrogen vacancy and halide interstitial defects in $MAPbI_3$. Using ab initio nonadiabatic molecular dynamics, we have revealed that $H_{v\text{-}N}$ introduces a defect state into the valence band near the VBM, while the defect state contributed by $H_{v\text{-}C}$ evolves from a shallow level to a deep level as temperature is raised from 0K to ambient conditions. Both $H_{v\text{-}N}$ and $H_{v\text{-}C}$ exhibit strong Lewis basicity and environmental activity, and are capable of capturing I_i in the perovskite lattice, thereby passivating I_i defects. The activity of $H_{v\text{-}C}$ is more pronounced, resulting in stronger bonding with I_i and better passivation. The carrier lifetimes of the I_i system passivated by H_v are notably longer than the carrier lifetimes in the systems with the defects and even pristine $MAPbI_3$. The self-passivation of $H_{v\text{-}C}$ and I_i enhances the carrier lifetime by over an order of magnitude. These findings are rationalized atomistically by considering in detail the structural and electronic properties of the materials, their atomic motions, and inelastic and elastic electron-vibrational interactions. The reported results demonstrate that a judicious and simultaneous control of the relative concentrations of the H_v and I_i defects can eliminate charge traps arising from both defect types, thereby minimizing energy and charge losses. The self-passivation strategy demonstrated by the ab initio quantum dynamics simulations is a promising route to improve the properties of organic−inorganic halide perovskites and other solar energy and optoelectronic materials. The reported study advances our understanding of defects in modern materials and devices.

■ ASSOCIATED CONTENT

Supporting Information

The Supporting Information is available free of charge at https://pubs.acs.org/doi/10.1021/jacs.4c12634.

Evolution of C−N distances of MA (H_v) in pristine $MAPbI_3$, $H_{v\text{-}N}$@$MAPbI_3$, and $H_{v\text{-}C}$@$MAPbI_3$; distributions of ∠Pb−I−Pb in $H_{v\text{-}N}$@$MAPbI_3$, $H_{v\text{-}C}$@$MAPbI_3$, pristine $MAPbI_3$, $H_{v\text{-}N}I_i$@$MAPbI_3$, and $H_{v\text{-}C}I_i$@$MAPbI_3$; evolutions of VBM, trap, and CBM state energies in $H_{v\text{-}N}$@$MAPbI_3$ and $H_{v\text{-}C}$@$MAPbI_3$ during AIMD simulation; diagram of trap-assisted carrier recombination; and evolution of key state populations in I_i@$MAPbI_3$, $H_{v\text{-}N}$@$MAPbI_3$, and $H_{v\text{-}C}$@$MAPbI_3$, obtained using short-time NA-MD simulations (PDF)

■ AUTHOR INFORMATION

Corresponding Authors

Oleg V. Prezhdo − *Department of Chemistry, University of Southern California, Los Angeles, California 90089, United States; Department of Physics and Astronomy, University of Southern California, Los Angeles, California 90089, United States;* orcid.org/0000-0002-5140-7500; Email: prezhdo@usc.edu

Run Long − *College of Chemistry, Key Laboratory of Theoretical & Computational Photochemistry of Ministry of Education, Beijing Normal University, Beijing 100875, PR China;* orcid.org/0000-0003-3912-8899; Email: runlong@bnu.edu.cn

Authors

Xinbo Ma − *College of Chemistry, Key Laboratory of Theoretical & Computational Photochemistry of Ministry of Education, Beijing Normal University, Beijing 100875, PR China*

Xuesong Tian − *College of Chemistry, Key Laboratory of Theoretical & Computational Photochemistry of Ministry of Education, Beijing Normal University, Beijing 100875, PR China*

Elizabeth Stippell − *Department of Chemistry, University of Southern California, Los Angeles, California 90089, United States*

Wei-Hai Fang − *College of Chemistry, Key Laboratory of Theoretical & Computational Photochemistry of Ministry of Education, Beijing Normal University, Beijing 100875, PR China;* orcid.org/0000-0002-1668-465X

Complete contact information is available at: https://pubs.acs.org/10.1021/jacs.4c12634

Notes

The authors declare no competing financial interest.

■ ACKNOWLEDGMENTS

This work was supported by the National Natural Science Foundation of China (grant nos. 92372121 and 22288201). R.L. acknowledges the Fundamental Research Funds for the Central Universities. O.V.P. acknowledges support of the US National Science Foundation (grant no. CHE-2154367).

■ REFERENCES

(1) Kojima, A.; Teshima, K.; Shirai, Y.; Miyasaka, T. Organometal Halide Perovskites as Visible-Light Sensitizers for Photovoltaic Cells. *J. Am. Chem. Soc.* **2009**, *131*, 6050−6051.

(2) Kim, M.; Jeong, J.; Lu, H.; Lee, T. K.; Eickemeyer, F. T.; Liu, Y.; Choi, I. W.; Choi, S. J.; Jo, Y.; Kim, H. B.; Mo, S. I.; Kim, Y. K.; Lee, H.; An, N. G.; Cho, S.; Tress, W. R.; Zakeeruddin, S. M.; Hagfeldt, A.; Kim, J. Y.; Gratzel, M.; Kim, D. S. Conformal Quantum Dot-SnO_2 Layers as Electron Transporters for Efficient Perovskite Solar Cells. *Science* **2022**, *375*, 302−306.

(3) Spanopoulos, I.; Hadar, I.; Ke, W.; Guo, P.; Mozur, E. M.; Morgan, E.; Wang, S.; Zheng, D.; Padgaonkar, S.; Manjunatha Reddy, G. N.; Weiss, E. A.; Hersam, M. C.; Seshadri, R.; Schaller, R. D.; Kanatzidis, M. G. Tunable Broad Light Emission from 3d "Hollow" Bromide Perovskites through Defect Engineering. *J. Am. Chem. Soc.* **2021**, *143*, 7069−7080.

(4) Feng, H.-J.; Paudel, T. R.; Tsymbal, E. Y.; Zeng, X. C. Tunable Optical Properties and Charge Separation in $CH_3NH_3Sn_xPb_{1-x}I_3$/TiO_2-Based Planar Perovskites Cells. *J. Am. Chem. Soc.* **2015**, *137*, 8227−8236.

(5) De Wolf, S.; Holovsky, J.; Moon, S. J.; Loper, P.; Niesen, B.; Ledinsky, M.; Haug, F. J.; Yum, J. H.; Ballif, C. Organometallic Halide Perovskites: Sharp Optical Absorption Edge and Its Relation to Photovoltaic Performance. *J. Phys. Chem. Lett.* **2014**, *5*, 1035−1039.

(6) Ghosh, T.; Aharon, S.; Etgar, L.; Ruhman, S. Free Carrier Emergence and Onset of Electron−Phonon Coupling in Methyl-

ammonium Lead Halide Perovskite Films. *J. Am. Chem. Soc.* **2017**, *139*, 18262−18270.
(7) Miyata, A.; Mitioglu, A.; Plochocka, P.; Portugall, O.; Wang, J. T.-W.; Stranks, S. D.; Snaith, H. J.; Nicholas, R. J. Direct Measurement of the Exciton Binding Energy and Effective Masses for Charge Carriers in Organic−Inorganic Tri-Halide Perovskites. *Nat. Phys.* **2015**, *11*, 582−587.
(8) Agiorgousis, M. L.; Sun, Y. Y.; Zeng, H.; Zhang, S. Strong Covalency-Induced Recombination Centers in Perovskite Solar Cell Material $CH_3NH_3PbI_3$. *J. Am. Chem. Soc.* **2014**, *136*, 14570−14575.
(9) Buin, A.; Pietsch, P.; Xu, J.; Voznyy, O.; Ip, A. H.; Comin, R.; Sargent, E. H. Materials Processing Routes to Trap-Free Halide Perovskites. *Nano Lett.* **2014**, *14*, 6281−6286.
(10) du Fossé, I.; Mulder, J. T.; Almeida, G.; Spruit, A. G. M.; Infante, I.; Grozema, F. C.; Houtepen, A. J. Limits of Defect Tolerance in Perovskite Nanocrystals: Effect of Local Electrostatic Potential on Trap States. *J. Am. Chem. Soc.* **2022**, *144*, 11059−11063.
(11) Shamsi, J.; Urban, A. S.; Imran, M.; De Trizio, L.; Manna, L. Metal Halide Perovskite Nanocrystals: Synthesis, Post-Synthesis Modifications, and Their Optical Properties. *Chem. Rev.* **2019**, *119*, 3296−3348.
(12) Park, J.; Kim, J.; Yun, H.-S.; Paik, M. J.; Noh, E.; Mun, H. J.; Kim, M. G.; Shin, T. J.; Seok, S. I. Controlled Growth of Perovskite Layers with Volatile Alkylammonium Chlorides. *Nature* **2023**, *616*, 724−730.
(13) Zhao, Y.; Ma, F.; Qu, Z.; Yu, S.; Shen, T.; Deng, H.-X.; Chu, X.; Peng, X.; Yuan, Y.; Zhang, X.; You, J. Inactive $(PbI_2)_2$ RbCl Stabilizes Perovskite Films for Efficient Solar Cells. *Science* **2022**, *377*, 531−534.
(14) Lu, H.; Liu, Y.; Ahlawat, P.; Mishra, A.; Tress, W. R.; Eickemeyer, F. T.; Yang, Y.; Fu, F.; Wang, Z.; Avalos, C. E.; et al. Vapor-Assisted Deposition of Highly Efficient, Stable Black-Phase $FAPbI_3$ Perovskite Solar Cells. *Science* **2020**, *370*, No. eabb8985.
(15) Xiong, Z.; Lan, L.; Wang, Y.; Lu, C.; Qin, S.; Chen, S.; Zhou, L.; Zhu, C.; Li, S.; Meng, L.; Sun, K.; Li, Y. Multifunctional Polymer Framework Modified SnO_2 Enabling a Photostable A-$FAPbI_3$ Perovskite Solar Cell with Efficiency Exceeding 23%. *ACS Energy Lett.* **2021**, *6*, 3824−3830.
(16) Zhang, D.; Zhang, H.; Guo, H.; Ye, F.; Liu, S.; Wu, Y. Stable A-$FAPbI_3$ in Inverted Perovskite Solar Cells with Efficiency Exceeding 22% Via a Self-Passivation Strategy. *Adv. Funct. Mater.* **2022**, *32*, 2200174.
(17) Zhang, H.; Ren, Z.; Liu, K.; Qin, M.; Wu, Z.; Shen, D.; Zhang, Y.; Chandran, H. T.; Hao, J.; Lee, C. S.; et al. Controllable Heterogenous Seeding-Induced Crystallization for High-Efficiency $FAPbI_3$ -Based Perovskite Solar Cells Over 24%. *Adv. Mater.* **2022**, *34*, No. e2204366.
(18) Zhang, J.; Jiang, X.; Liu, X.; Guo, X.; Li, C. Maximizing Merits of Undesirable δ-$FAPbI_3$ by Constructing Yellow/Black Heterophase Bilayer for Efficient and Stable Perovskite Photovoltaics. *Adv. Funct. Mater.* **2022**, *32*, 2204642.
(19) Yin, W.-J.; Shi, T.; Yan, Y. Unusual Defect Physics in $CH_3NH_3PbI_3$ Perovskite Solar Cell Absorber. *Appl. Phys. Lett.* **2014**, *104* (6), 063903.
(20) Caselli, V. M.; Wei, Z.; Ackermans, M. M.; Hutter, E. M.; Ehrler, B.; Savenije, T. J. Charge Carrier Dynamics Upon Sub-Bandgap Excitation in Methylammonium Lead Iodide Thin Films: Effects of Urbach Tail, Deep Defects, and Two-Photon Absorption. *ACS Energy Lett.* **2020**, *5*, 3821−3827.
(21) Keeble, D. J.; Wiktor, J.; Pathak, S. K.; Phillips, L. J.; Dickmann, M.; Durose, K.; Snaith, H. J.; Egger, W. Identification of Lead Vacancy Defects in Lead Halide Perovskites. *Nat. Commun.* **2021**, *12*, 5566.
(22) Musiienko, A.; Ceratti, D. R.; Pipek, J.; Brynza, M.; Elhadidy, H.; Belas, E.; Betušiak, M.; Delport, G.; Praus, P. Defects in Hybrid Perovskites: The Secret of Efficient Charge Transport. *Adv. Funct. Mater.* **2021**, *31*, 2104467.
(23) Cheng, W.; He, X.; Wang, J. G.; Tian, W.; Li, L. N -(2-aminoethyl) Acetamide Additive Enables Phase-Pure and Stable α-$FAPbI_3$ for Efficient Self-Powered Photodetectors. *Adv. Mater.* **2022**, *34*, No. e2208325.
(24) Oner, S. M.; Sezen, E.; Yordanli, M. S.; Karakoc, E.; Deger, C.; Yavuz, I. Surface Defect Formation and Passivation in Formamidinium Lead Triiodide ($FAPbI_3$) Perovskite Solar Cell Absorbers. *J. Phys. Chem. Lett.* **2022**, *13*, 324−330.
(25) Wang, T.; Li, Y.; Cao, Q.; Yang, J.; Yang, B.; Pu, X.; Zhang, Y.; Zhao, J.; Zhang, Y.; Chen, H.; Hagfeldt, A.; Li, X. Deep Defect Passivation and Shallow Vacancy Repair Via an Ionic Silicone Polymer toward Highly Stable Inverted Perovskite Solar Cells. *Energy Environ. Sci.* **2022**, *15*, 4414−4424.
(26) Liu, D. Y.; Wu, Y. F.; Vasenko, A. S.; Prezhdo, O. V. Grain Boundary Sliding and Distortion on a Nanosecond Timescale Induce Trap States in $CsPbBr_3$: Ab Initio Investigation with Machine Learning Force Field. *Nanoscale* **2022**, *15*, 285−293.
(27) Prezhdo, O. V.; Wu, Y. F.; Liu, D. Y.; Chu, W. B.; Wang, B. P.; Vasenko, A. S. Fluctuations at Metal Halide Perovskite Grain Boundaries Create Transient Trap States: Machine Learning Assisted Ab Initio Analysis. *ACS Appl. Mater. Interfaces* **2022**, *14*, 55753−55761.
(28) Zheng, X.; Chen, B.; Dai, J.; Fang, Y.; Bai, Y.; Lin, Y.; Wei, H.; Zeng, X. C.; Huang, J. Defect Passivation in Hybrid Perovskite Solar Cells Using Quaternary Ammonium Halide Anions and Cations. *Nat. Energy* **2017**, *2*, 17102.
(29) Chen, B.; Rudd, P. N.; Yang, S.; Yuan, Y.; Huang, J. Imperfections and Their Passivation in Halide Perovskite Solar Cells. *Chem. Soc. Rev.* **2019**, *48*, 3842−3867.
(30) Tan, S.; Yavuz, I.; Weber, M. H.; Huang, T.; Chen, C.-H.; Wang, R.; Wang, H.-C.; Ko, J. H.; Nuryyeva, S.; Xue, J.; Zhao, Y.; Wei, K.-H.; Lee, J.-W.; Yang, Y. Shallow Iodine Defects Accelerate the Degradation of A-Phase Formamidinium Perovskite. *Joule* **2020**, *4*, 2426−2442.
(31) Kang, D.-H.; Kim, S.-Y.; Lee, J.-W.; Park, N.-G. Efficient Surface Passivation of Perovskite Films by a Post-Treatment Method with a Minimal Dose. *J. Mater. Chem. A* **2021**, *9*, 3441−3450.
(32) Lee, S.-H.; Jeong, S.; Seo, S.; Shin, H.; Ma, C.; Park, N.-G. Acid Dissociation Constant: A Criterion for Selecting Passivation Agents in Perovskite Solar Cells. *ACS Energy Lett.* **2021**, *6*, 1612−1621.
(33) Zhang, X.; Shen, J. X.; Turiansky, M. E.; Van de Walle, C. G. Minimizing Hydrogen Vacancies to Enable Highly Efficient Hybrid Perovskites. *Nat. Mater.* **2021**, *20*, 971−976.
(34) Liu, Z.; Duan, C.; Liu, F.; Chan, C. C. S.; Zhu, H.; Yuan, L.; Li, J.; Li, M.; Zhou, B.; Wong, K. S.; et al. Perovskite Bifunctional Diode with High Photovoltaic and Electroluminescent Performance by Holistic Defect Passivation. *Small* **2022**, *18*, No. e2105196.
(35) Zhang, H.; Pfeifer, L.; Zakeeruddin, S. M.; Chu, J.; Gratzel, M. Tailoring Passivators for Highly Efficient and Stable Perovskite Solar Cells. *Nat. Rev. Chem.* **2023**, *7*, 632−652.
(36) Zhang, Z.; Qiao, L.; Meng, K.; Long, R.; Chen, G.; Gao, P. Rationalization of Passivation Strategies toward High-Performance Perovskite Solar Cells. *Chem. Soc. Rev.* **2023**, *52*, 163−195.
(37) Wang, R.; Xue, J.; Wang, K. L.; Wang, Z. K.; Luo, Y.; Fenning, D.; Xu, G.; Nuryyeva, S.; Huang, T.; Zhao, Y.; Yang, J. L.; Zhu, J.; Wang, M.; Tan, S.; Yavuz, I.; Houk, K. N.; Yang, Y. Constructive Molecular Configurations for Surface-Defect Passivation of Perovskite Photovoltaics. *Science* **2019**, *366*, 1509−1513.
(38) Guo, J.; Sun, J.; Hu, L.; Fang, S.; Ling, X.; Zhang, X.; Wang, Y.; Huang, H.; Han, C.; Cazorla, C.; et al. Indigo: A Natural Molecular Passivator for Efficient Perovskite Solar Cells. *Adv. Energy Mater.* **2022**, *12*, 2200537.
(39) Zhang, Z.; Gao, Y.; Li, Z.; Qiao, L.; Xiong, Q.; Deng, L.; Zhang, Z.; Long, R.; Zhou, Q.; Du, Y.; et al. Marked Passivation Effect of Naphthalene-1,8-Dicarboximides in High-Performance Perovskite Solar Cells. *Adv. Mater.* **2021**, *33*, No. e2008405.
(40) He, J.; Fang, W.-H.; Long, R. Unravelling the Effects of Oxidation State of Interstitial Iodine and Oxygen Passivation on Charge Trapping and Recombination in $CH_3NH_3PbI_3$ Perovskite: A Time-Domain Ab Initio Study. *Chem. Sci.* **2019**, *10*, 10079−10088.

https://doi.org/10.1021/jacs.4c12634
J. Am. Chem. Soc. 2024, 146, 29255−29265

(41) He, J.; Fang, W.-H.; Long, R.; Prezhdo, O. V. Bidentate Lewis Bases Are Preferred for Passivation of $MAPbI_3$ Surfaces: A Time-Domain Ab Initio Analysis. *Nano Energy* **2021**, *79*, 105491.
(42) Liu, L.; Fang, W. H.; Long, R.; Prezhdo, O. V. Lewis Base Passivation of Hybrid Halide Perovskites Slows Electron-Hole Recombination: Time-Domain Ab Initio Analysis. *J. Phys. Chem. Lett.* **2018**, *9*, 1164−1171.
(43) Qiao, L.; Fang, W. H.; Long, R. The Interplay between Lead Vacancy and Water Rationalizes the Puzzle of Charge Carrier Lifetimes in $CH_3NH_3PbI_3$: Time-Domain Ab Initio Analysis. *Angew. Chem., Int. Ed.* **2020**, *59*, 13347−13353.
(44) Qiao, L.; Fang, W. H.; Long, R.; Prezhdo, O. V. Elimination of Charge Recombination Centers in Metal Halide Perovskites by Strain. *J. Am. Chem. Soc.* **2021**, *143*, 9982−9990.
(45) Qiao, L.; Fang, W. H.; Prezhdo, O. V.; Long, R. Suppressing Oxygen-Induced Deterioration of Metal Halide Perovskites by Alkaline Earth Metal Doping: A Quantum Dynamics Study. *J. Am. Chem. Soc.* **2022**, *144*, 5543−5551.
(46) Shi, R.; Fang, W.-H.; Vasenko, A. S.; Long, R.; Prezhdo, O. V. Efficient Passivation of Dy Center in $CH_3NH_3PbBr_3$ by Chlorine: Quantum Molecular Dynamics. *Nano Res.* **2022**, *15*, 2112−2122.
(47) Shi, R.; Long, R. Atomic Model for Alkali Metal-Doped Tin-Lead Mixed Perovskites: Insight from Quantum Dynamics. *J. Phys. Chem. Lett.* **2023**, *14*, 2878−2885.
(48) Liu, D. Y.; Wu, Y. F.; Samatov, M. R.; Vasenko, A. S.; Chulkov, E. V.; Prezhdo, O. V. Compression Eliminates Charge Traps by Stabilizing Perovskite Grain Boundary Structures: An Ab Initio Analysis with Machine Learning Force Field. *Chem. Mater.* **2024**, *36*, 2898−2906.
(49) Li, W.; She, Y. L.; Vasenko, A. S.; Prezhdo, O. V. Ab Initio Nonadiabatic Molecular Dynamics of Charge Carriers in Metal Halide Perovskites. *Nanoscale* **2021**, *13*, 10239−10265.
(50) Long, R.; Liu, J.; Prezhdo, O. V. Unravelling the Effects of Grain Boundary and Chemical Doping on Electron-Hole Recombination in $CH_3NH_3PbI_3$ Perovskite by Time-Domain Atomistic Simulation. *J. Am. Chem. Soc.* **2016**, *138*, 3884−3890.
(51) Qiao, L.; Fang, W.-H.; Long, R.; Prezhdo, O. V. Atomic Model for Alkali Metal Passivation of Point Defects at Perovskite Grain Boundaries. *ACS Energy Lett.* **2020**, *5*, 3813−3820.
(52) Liang, Y.; Cui, X.; Li, F.; Stampfl, C.; Ringer, S. P.; Huang, J.; Zheng, R. Minimizing and Controlling Hydrogen for Highly Efficient Formamidinium Lead Triiodide Solar Cells. *J. Am. Chem. Soc.* **2022**, *144*, 6770−6778.
(53) Prezhdo, O. V. Modeling Non-Adiabatic Dynamics in Nanoscale and Condensed Matter Systems. *Acc. Chem. Res.* **2021**, *54*, 4239−4249.
(54) Jasper, A. W.; Nangia, S.; Zhu, C.; Truhlar, D. G. Non-Born−Oppenheimer Molecular Dynamics. *Acc. Chem. Res.* **2006**, *39*, 101−108.
(55) Crespo-Otero, R.; Barbatti, M. Recent Advances and Perspectives on Nonadiabatic Mixed Quantum-Classical Dynamics. *Chem. Rev.* **2018**, *118*, 7026−7068.
(56) Mai, S.; Marquetand, P.; González, L. Nonadiabatic Dynamics: The Sharc Approach. *WIREs Comput. Mol. Sci.* **2018**, *8*, No. e1370.
(57) Zheng, Q.; Chu, W.; Zhao, C.; Zhang, L.; Guo, H.; Wang, Y.; Jiang, X.; Zhao, J. Ab Initio Nonadiabatic Molecular Dynamics Investigations on the Excited Carriers in Condensed Matter Systems. *WIREs Comput. Mol. Sci.* **2019**, *9* (6), No. e1411.
(58) Jaeger, H. M.; Fischer, S.; Prezhdo, O. V. Decoherence-Induced Surface Hopping. *J. Chem. Phys.* **2012**, *137* (22), 22A545.
(59) Liu, D.; Wang, B.; Vasenko, A.; Prezhdo, O. V. Decoherence Ensures Convergence of Non-Adiabatic Molecular Dynamics with Number of States. *J. Chem. Phys.* **2024**, *161* (6), 064104.
(60) Craig, C. F.; Duncan, W. R.; Prezhdo, O. V. Trajectory Surface Hopping in the Time-Dependent Kohn-Sham Approach for Electron-Nuclear Dynamics. *Phys. Rev. Lett.* **2005**, *95*, 163001.
(61) Fischer, S. A.; Habenicht, B. F.; Madrid, A. B.; Duncan, W. R.; Prezhdo, O. V. Regarding the validity of the time-dependent Kohn−Sham approach for electron-nuclear dynamics via trajectory surface hopping. *J. Chem. Phys.* **2011**, *134*, 024102.
(62) Akimov, A. V.; Prezhdo, O. V. Advanced Capabilities of the Pyxaid Program: Integration Schemes, Decoherence Effects, Multi-excitonic States, and Field-Matter Interaction. *J. Chem. Theory Comput.* **2014**, *10*, 789−804.
(63) Gumber, S.; Prezhdo, O. V. Zeno and Anti-Zeno Effects in Nonadiabatic Molecular Dynamics. *J. Phys. Chem. Lett.* **2023**, *14*, 7274−7282.
(64) Prezhdo, O. V. Mean Field Approximation for the Stochastic Schrödinger Equation. *J. Chem. Phys.* **1999**, *111*, 8366−8377.
(65) Mukamel, S. *Principles of Nonlinear Optical Spectroscopy*; Oxford University Press, 1995.
(66) Akimov, A. V.; Prezhdo, O. V. The Pyxaid Program for Non-Adiabatic Molecular Dynamics in Condensed Matter Systems. *J. Chem. Theory Comput.* **2013**, *9*, 4959−4972.
(67) Li, L.; Long, R.; Prezhdo, O. V. Why Chemical Vapor Deposition Grown MoS_2 Samples Outperform Physical Vapor Deposition Samples: Time-Domain Ab Initio Analysis. *Nano Lett.* **2018**, *18*, 4008−4014.
(68) Ma, X.; Fang, W. H.; Long, R.; Prezhdo, O. V. Compression of Organic Molecules Coupled with Hydrogen Bonding Extends the Charge Carrier Lifetime in Ba_2Sn_4. *J. Am. Chem. Soc.* **2024**, *146*, 16314−16323.
(69) Wu, Y.; Chu, W.; Vasenko, A. S.; Prezhdo, O. V. Common Defects Accelerate Charge Carrier Recombination in $CsSnI_3$ without Creating Mid-Gap States. *J. Phys. Chem. Lett.* **2021**, *12*, 8699−8705.
(70) Zhu, Y.; Prezhdo, O. V.; Long, R.; Fang, W.-H. Twist Angle-Dependent Intervalley Charge Carrier Transfer and Recombination in Bilayer WS_2. *J. Am. Chem. Soc.* **2023**, *145*, 22826−22835.
(71) Chaban, V. V.; Prezhdo, V. V.; Prezhdo, O. V. Covalent Linking Greatly Enhances Photoinduced Electron Transfer in Fullerene-Quantum Dot Nanocomposites: Time-Domain Ab Initio Study. *J. Phys. Chem. Lett.* **2013**, *4*, 1−6.
(72) Cheng, C.; Fang, W. H.; Long, R.; Prezhdo, O. V. Water Splitting with a Single-Atom Cu/TiO_2 Photocatalyst: Atomistic Origin of High Efficiency and Proposed Enhancement by Spin Selection. *JACS Au* **2021**, *1*, 550−559.
(73) Zhang, L. L.; Vasenko, A. S.; Zhao, J.; Prezhdo, O. V. Mono-Elemental Properties of 2d Black Phosphorus Ensure Extended Charge Carrier Lifetimes under Oxidation: Time-Domain Ab Initio Analysis. *J. Phys. Chem. Lett.* **2019**, *10*, 1083−1091.
(74) Zhang, Z. S.; Liu, L. H.; Fang, W. H.; Long, R.; Tokina, M. V.; Prezhdo, O. V. Plasmon-Mediated Electron Injection from Au Nanorods into MoS_2: Traditional Versus Photoexcitation Mechanism. *Chem* **2018**, *4*, 1112−1127.
(75) Giri, A.; Walton, S. G.; Tomko, J.; Bhatt, N.; Johnson, M. J.; Boris, D. R.; Lu, G. Y.; Caldwell, J. D.; Prezhdo, O. V.; Hopkins, P. E. Ultrafast and Nanoscale Energy Transduction Mechanisms and Coupled Thermal Transport across Interfaces. *ACS Nano* **2023**, *17*, 14253−14282.
(76) Li, W.; Xue, T.; Mora-Perez, C.; Prezhdo, O. V. Ab Initio Quantum Dynamics of Plasmonic Charge Carriers. *Trends Chem.* **2023**, *5*, 634−645.
(77) Kresse, G.; Hafner, J. Ab Initio Molecular Dynamics for Liquid Metals. *Phys. Rev. B: Condens. Matter* **1993**, *47*, 558−561.
(78) Blöchl, P. E. Projector Augmented-Wave Method. *Phys. Rev. B* **1994**, *50*, 17953−17979.
(79) Perdew, J. P.; Burke, K.; Ernzerhof, M. Generalized Gradient Approximation Made Simple. *Phys. Rev. Lett.* **1996**, *77*, 3865−3868.
(80) Monkhorst, H. J.; Pack, J. D. Special Points for Brillouin-Zone Integrations. *Phys. Rev. B* **1976**, *13*, 5188−5192.
(81) Grimme, S. Semiempirical GGA-Type Density Functional Constructed with a Long-Range Dispersion Correction. *J. Comput. Chem.* **2006**, *27*, 1787−1799.
(82) Chu, W. B.; Prezhdo, O. V. Concentric Approximation for Fast and Accurate Numerical Evaluation of Nonadiabatic Coupling with Projector Augmented-Wave Pseudopotentials. *J. Phys. Chem. Lett.* **2021**, *12*, 3082−3089.

https://doi.org/10.1021/jacs.4c12634
J. Am. Chem. Soc. 2024, 146, 29255−29265

(83) Chu, W. B.; Zheng, Q. J.; Akimov, A. V.; Zhao, J.; Saidi, W. A.; Prezhdo, O. V. Accurate Computation of Nonadiabatic Coupling with Projector Augmented-Wave Pseudopotentials. *J. Phys. Chem. Lett.* **2020**, *11*, 10073−10080.
(84) Quarti, C.; Grancini, G.; Mosconi, E.; Bruno, P.; Ball, J. M.; Lee, M. M.; Snaith, H. J.; Petrozza, A.; De Angelis, F. The Raman Spectrum of the $CH_3NH_3PbI_3$ Hybrid Perovskite: Interplay of Theory and Experiment. *J. Phys. Chem. Lett.* **2014**, *5*, 279−284.
(85) Leguy, A. M. A.; Goñi, A. R.; Frost, J. M.; Skelton, J.; Brivio, F.; Rodríguez-Martínez, X.; Weber, O. J.; Pallipurath, A.; Alonso, M. I.; Campoy-Quiles, M.; Weller, M. T.; Nelson, J.; Walsh, A.; Barnes, P. R. F. Dynamic Disorder, Phonon Lifetimes, and the Assignment of Modes to the Vibrational Spectra of Methylammonium Lead Halide Perovskites. *Phys. Chem. Chem. Phys.* **2016**, *18*, 27051−27066.
(86) Liu, D.; Wang, B.; Wu, Y.; Vasenko, A. S.; Prezhdo, O. V. Breaking the Size Limitation of Nonadiabatic Molecular Dynamics in Condensed Matter Systems with Local Descriptor Machine Learning. *Proc. Natl. Acad. Sci. U. S. A.* **2024**, *121*, No. e2403497121.
(87) Agrawal, S.; Wang, B. P.; Wu, Y. F.; Casanova, D.; Prezhdo, O. V. Photocatalytic Activity of Dual Defect Modified Graphitic Carbon Nitride Is Robust to Tautomerism: Machine Learning Assisted Ab Initio Quantum Dynamics. *Nanoscale* **2024**, *16*, 8986−8995.

https://doi.org/10.1021/jacs.4c12634
J. Am. Chem. Soc. 2024, 146, 29255−29265